

# Shallow low-velocity zone of the San Jacinto fault from local earthquake waveform modelling

Hongfeng Yang and Lupei Zhu

Department of Earth and Atmospheric Sciences, Saint Louis University, St Louis, MO 63108, USA. E-mail: hyang4@slu.edu

Accepted 2010 July 16. Received 2010 July 13; in original form 2010 March 23

## SUMMARY

We developed a method to determine the depth extent of low-velocity zone (LVZ) associated with a fault zone (FZ) using *S*-wave precursors from local earthquakes. The precursors are diffracted *S* waves around the edges of LVZ and their relative amplitudes to the direct *S* waves are sensitive to the LVZ depth. We applied the method to data recorded by three temporary arrays across three branches of the San Jacinto FZ. The FZ dip was constrained by differential traveltimes of *P* waves between stations at two side of the FZ. Other FZ parameters (width and velocity contrast) were determined by modelling waveforms of direct and FZ-reflected *P* and *S* waves. We found that the LVZ of the Buck Ridge fault branch has a width of  $\sim 150$  m with a 30–40 per cent reduction in  $V_p$  and a 50–60 per cent reduction in  $V_s$ . The fault dips  $70 \pm 5^\circ$  to southwest and its LVZ extends only to  $2 \pm 1$  km in depth. The LVZ of the Clark Valley fault branch has a width of  $\sim 200$  m with 40 per cent reduction in  $V_p$  and 50 per cent reduction in  $V_s$ . The Coyote Creek branch is nearly vertical and has a LVZ of  $\sim 150$  m in width and of 25 per cent reduction in  $V_p$  and 50 per cent reduction in  $V_s$ . The LVZs of these three branches are not centred at the surface fault trace but are located to their northeast, indicating asymmetric damage during earthquakes.

**Key words:** Body waves; Interface waves; Wave scattering and diffraction; Wave propagation.

## 1 INTRODUCTION

Major crustal faults are usually characterized as a narrow zone of intense damage and deformation. A fault zone (FZ) usually includes a fault core (tens of centimetres to several meters in width) and the surrounding damage zone (hundreds of meters to several kilometres in width) (e.g. Chester *et al.* 1993; Evans & Chester 1995). The damage zone is generated by earthquakes over time and is seismically characterized as a low-velocity zone (LVZ) composed of highly fractured materials, breccia, clay and cataclases. Cracks in the damage zone may contain and transport fluids which play an important role on FZ strength related to earthquake generation and rupture distribution (Eberhart-Phillips *et al.* 1995). Moreover, the LVZ material may result in asymmetric damage patterns during an earthquake (e.g. Ben-Zion & Shi 2005; Dor *et al.* 2006) and could amplify the ground motion by a factor of 30 with realistic parameters (Ben-Zion & Aki 1990). Studies of damage zone healing after a large earthquake highlight its importance to understanding earthquake cycle and evolution of fault systems (Li *et al.* 1998; Vidale & Li 2003). Complex structure (geometrical and material properties) of FZ may control the earthquake rupture process and slip localization and is important to understanding the earthquake physics (e.g. Aki 1979; Scholz 1990; Kanamori 1994; Kanamori & Brodsky 2004).

Different geological and geophysical methods have been used to investigate the FZ structures. Studying exhumed faults can provide

direct information of FZ parameters but is limited in depth (Chester *et al.* 1993; Sieh *et al.* 1993; Johnson *et al.* 1994). Drilling in some particular sites, for example, SAFOD, can sample a FZ in depth directly but it is laterally limited. Seismic reflection and refraction surveys can image FZs down to a few kilometres but have difficulties to image very narrow, nearly vertical FZs (Eberhart-Phillips *et al.* 1995; Hole *et al.* 2001; Ben-Zion & Sammis 2003). Many other geophysical methods have also been used to study FZ properties at the seismogenic depth such as gravity and electromagnetic surveys, traveltome tomography, earthquake location, waveform modelling of earthquake body waves, FZ head waves and FZ trapped waves (e.g. Mooney & Ginzburg 1986; Ben-Zion & Malin 1991; Ben-Zion *et al.* 1992; Li *et al.* 2002; Prejean *et al.* 2002; Waldhauser & Ellsworth 2002; McGuire & Ben-Zion 2005; Bleibinhaus *et al.* 2007; Li *et al.* 2007; Zhao & Peng 2008; Yang *et al.* 2009). Among these methods, the most frequently used technique is to model the FZ trapped waves, which are low frequency wave trains with relatively large amplitude following the *S* wave. This method has been used on different faults around the world, such as the North Anatolian FZ in Turkey (Ben-Zion *et al.* 2003), the Nocera Umbra FZ in central Italy (Rovelli *et al.* 2002), the San Andreas FZ at Parkfield (Korneev *et al.* 2003; Li *et al.* 2004; Li & Malin 2008), the Lavic Lake FZ (Li *et al.* 2003), the Calico FZ (Cochran *et al.* 2009), the Landers FZ (Li *et al.* 1994, 1999, 2000; Peng *et al.* 2003) and the San Jacinto FZs in California (Li *et al.* 1997; Li & Vernon 2001; Lewis *et al.* 2005). Most FZ trapped wave studies revealed a LVZ ranged from

~75 to ~350 m with the shear wave velocity reduced by 20–50 per cent. However, uncertainties of trapped wave modelling results due to the non-uniqueness and trade-off among FZ parameters have been noted (Peng *et al.* 2003; Lewis *et al.* 2005). It is still under debate whether the trapped energy comes from a shallow LVZ structure or a deep one (Li *et al.* 1997; Li & Vernon 2001; Ben-Zion & Sammis 2003; Lewis *et al.* 2005). For example, a 15–20-km-deep LVZ of the San Jacinto FZ (SJFZ) was reported by Li & Vernon (2001) while another group using the same data set argued that it was only 3–5 km deep (Lewis *et al.* 2005).

A recent numerical analysis of FZ trapped wave pointed out that determination of FZ structure at seismogenic depth requires using higher frequency waveforms than the FZ trapped wave (Wu *et al.* 2008). In this study, we analyse high frequency body wave waveforms of local earthquakes recorded by temporary arrays across the three branches of the SJFZ. Using a recently developed method (Li *et al.* 2007), we determine FZ parameters of width and velocity drops. The FZ dip is determined by an analysis of spatial distribution of differential traveltimes of *P* waves across the arrays. In addition, we observe a precursor before the direct *S* wave caused by diffraction around the edge of LVZ. The amplitude ratios between the diffracted wave and the direct *S* wave are sensitive to the LVZ depth so that we can determine the depth by modelling their waveforms. We also estimate uncertainties of LVZ depth determination due to uncertainties of event locations by performing synthetic tests. Finally, we summarize the seis-

mic structures of the SJFZ by modelling the high frequency body waveforms.

## 2 THE 1999 SAN JACINTO FAULT ZONE SEISMIC EXPERIMENT

The San Jacinto fault is the most seismically active strand of the San Andreas fault system in southern California (Fig. 1), with successive occurrences of moderate earthquakes since 1890 (Sanders & Kanamori 1984; Sykes & Nishenko 1984). Study of sedimentary rocks in the Borrego Badlands, southern California, showed that the SJF was formed in the Pleistocene era, 1.0–1.1 Ma (Lutz *et al.* 2006). The average slip rate on the SJF is approximate 12–15 mm yr<sup>-1</sup> based on studies of Pleistocene and Holocene alluvial fans and fluvial deposits and the GPS measurements (Rockwell *et al.* 1990; Becker *et al.* 2005).

The southern portion of the SJF near Anza is composed of three branches: the Buck Ridge fault (BRF); the Clark Valley fault (CVF) and the Coyote Creek fault (CCF). In 1999, three linear seismic arrays were deployed across these fault strands (Fig. 1). Each array was 350 m in length and consisted of 12 three-component L22 2-Hz short-period instruments. The profiles were approximately perpendicular to the surface trace of the fault (Fig. 1). Array A across the CVF and array B across the BRF operated for 2 months while array C across the CCF was deployed for 4 months in the

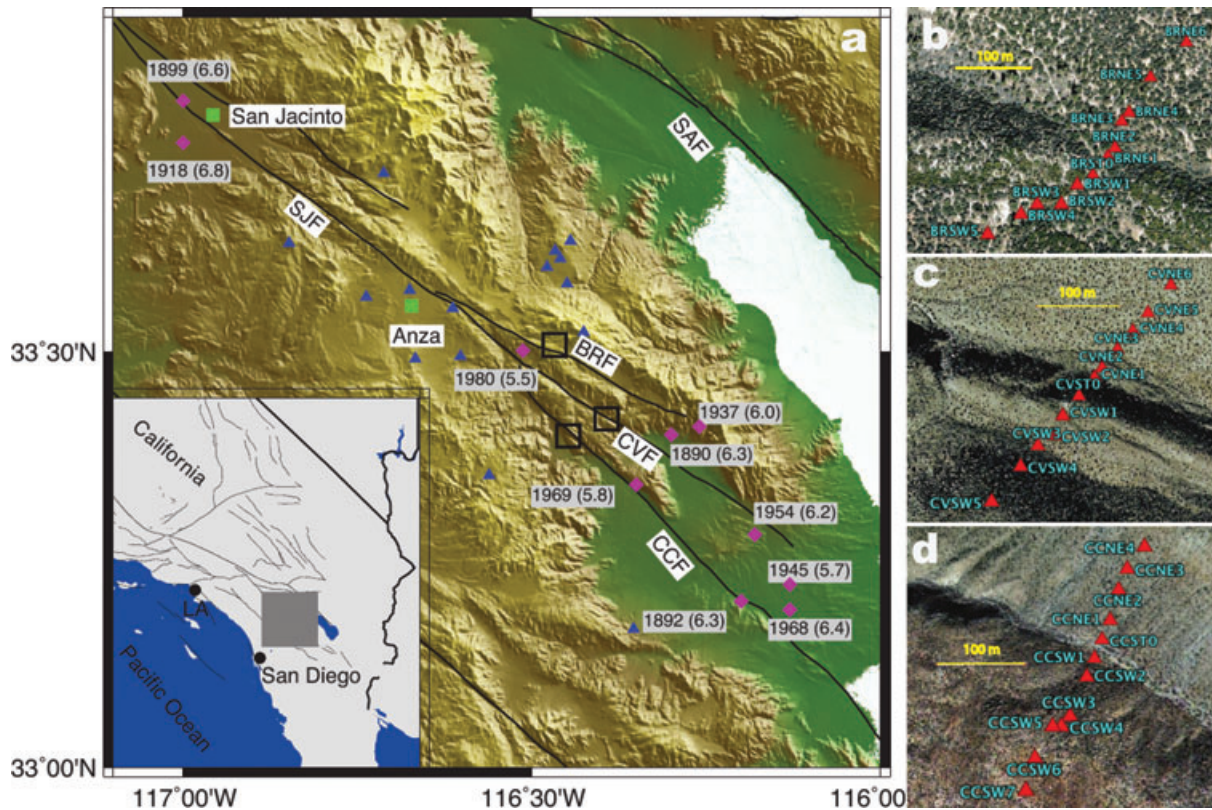


**Figure 1.** (a) Map showing the San Jacinto fault zone (SJFZ) and locations of nearby major historic earthquakes (diamonds, with year and magnitude indicated). The southern segment of the fault splits into three branches: the Buck Ridge branch (BRF), Clark Valley branch (CVF) and Coyote Creek branch (CCF). Three linear seismic arrays were deployed across these branches as shown by black squares. Blue triangles represents seismic stations of the Anza network. The inset map shows location of study area (shadowed area) and major faults in California (black lines). (b) A closeup view of geometry of the BRF array and local topography obtained from Google Earth (c) the CVF and (d) the CCF array.

## Event 4527

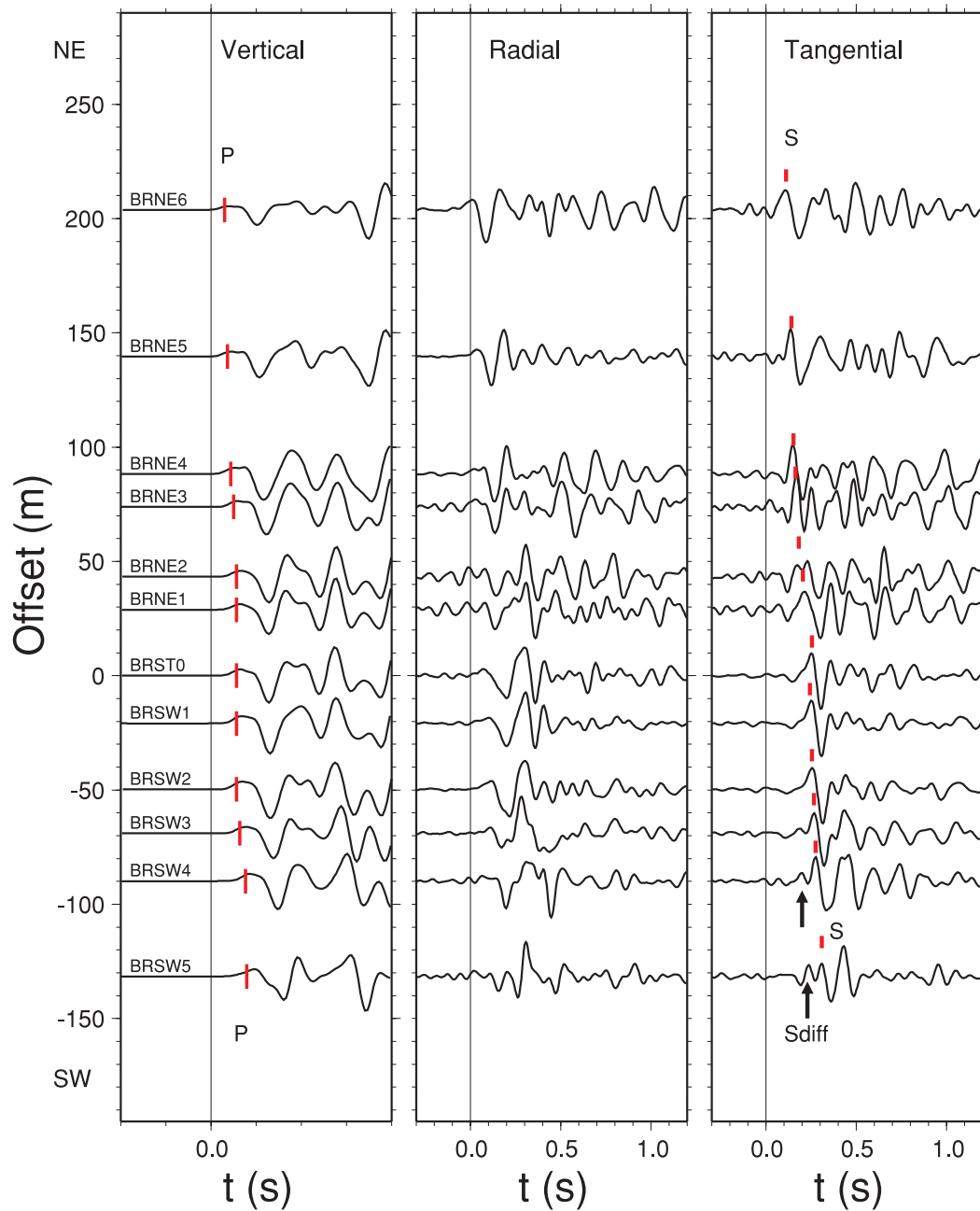


**Figure 2.** Three-component seismograms of event 4527 recorded by the seismic array across the BRF. From left to right are vertical component in  $P$  window, radial, and horizontal components in  $S$  window. The  $Y$ -axis stands for the offset from the central station of the array from southwest to northeast. Red bars represent the hand-picked  $P$ - and  $S$ -wave arrival times. Black arrows point to the diffracted  $S$ -wave phases before the direct  $S$  waves.

field. Waveforms of  $\sim 1500$  small earthquakes were recorded by the arrays during operation period. More details on the experiment were described in Li & Vernon (2001).

### 3 DATA ANALYSIS AND RESULTS

#### 3.1 FZ dip based on $P$ -wave arrival times

We selected events that have been relocated by Shearer *et al.* (2005). We required that events were within 10 km in epicentral distance

to the seismic array and were recorded by at least seven stations of the arrays. There were 52 such events for the BRF array, 41 for the CCF array and only 5 for the CVF array. We removed instrument responses and bandpass filtered the waveforms between 1 and 15 Hz. We then hand picked direct  $P$ - and  $S$ -wave arrival times for each event.

Fig. 2 shows three-component seismograms from one earthquake recorded by the BRF array. The event is located southwest of the surface fault trace (Fig. 3a). Usually the LVZ associated with a FZ causes the  $P$  and  $S$  waves to arrive later at stations on the other side of

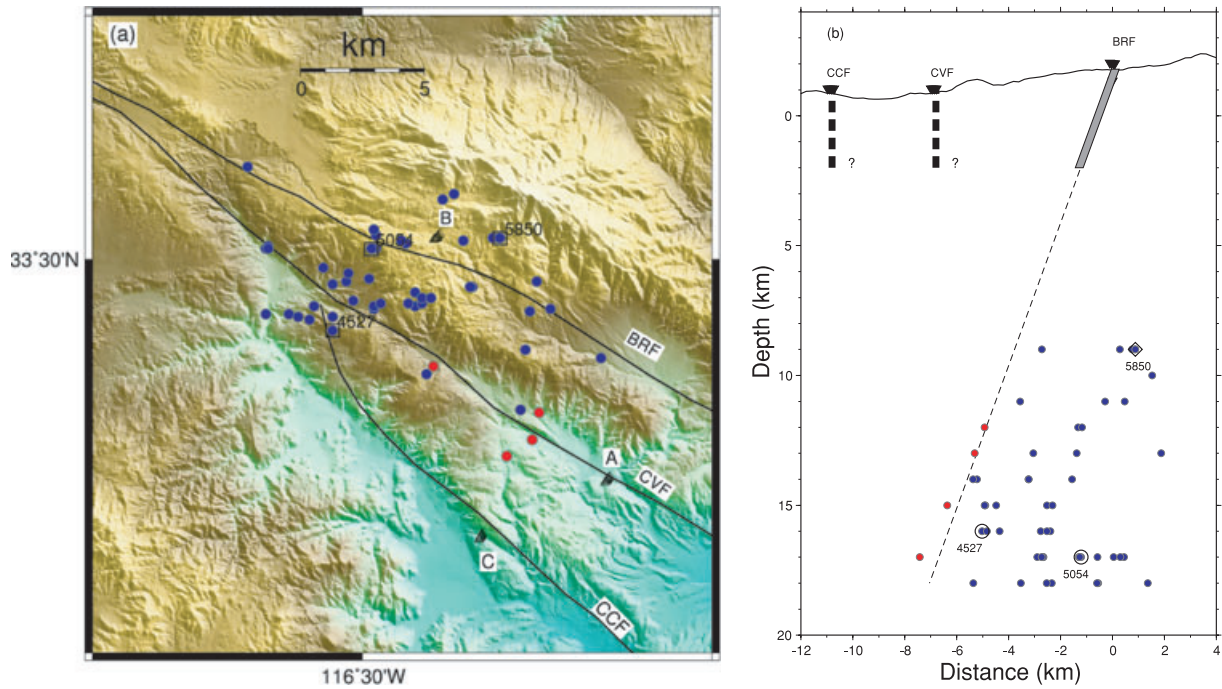


**Figure 3.** Map view (a) and cross-section (b) of locations of events recorded by the BRF array. Blue and red colours represent positive and negative *P*-wave traveltimes differences between the northeastern-most and southwestern-most stations of the array, respectively. For those events whose waveforms are shown in the paper, event numbers are marked on their locations. The grey bar represents the extent of LVZ of BRF. Thick dashed lines stand for LVZs of the CCF and the CVF. BRF, the Buck Ridge fault; CVF, the Clark Valley fault and CCF, the Coyote Creek fault.

the fault. However, Fig. 2 shows that the direct *P* and *S* waves arrived earlier at northeastern stations than at the southwestern stations. This indicates that the LVZ is not vertical but dips to the southwest so that the event is actually located on the northeastern side of the LVZ (Fig. 3b).

In Fig. 3, we show event locations and the *P* arrival time differences between the northeastern-most and southwestern-most stations of the BRF array. Out of 52 events, only four events located south of the array show early *P* arrivals at southwestern stations, that is, on the southwestern side of the LVZ. The rest are located on the northeastern side of the LVZ. This allowed us to determine the dip of the LVZ in the cross-section perpendicular to the strike of the BRF (Fig. 3b). The best-fitting plane shows that BRF dips 70° to the southwest. Using the same analysis we found that CCF is nearly vertical. The dip of CVF could not be determined due to lack of events.

Since we constrained the LVZ dip by the spatial distribution of earthquakes, uncertainty of event locations will lead to uncertainty in dip of the LVZ. Most events used in this study have relatively small uncertainties laterally and in depth. We applied 1 km perturbation to event locations and found the uncertainty of the corresponding LVZ dip was less than 5°. Therefore, we concluded that the BRF dips  $70 \pm 5^\circ$  to the southwest.

### 3.2 FZ widths and velocity drops

Recently, we developed a technique to determine high-resolution FZ structure using arrival times and waveforms of FZ transmitted and reflected *P* and *S* body waves from local earthquakes (Li *et al.* 2007). As shown in Fig. 4, a LVZ that embedded into a uniform half-space can generate FZ-reflected body waves for an event near the FZ. When the event is close to the FZ, the differential times

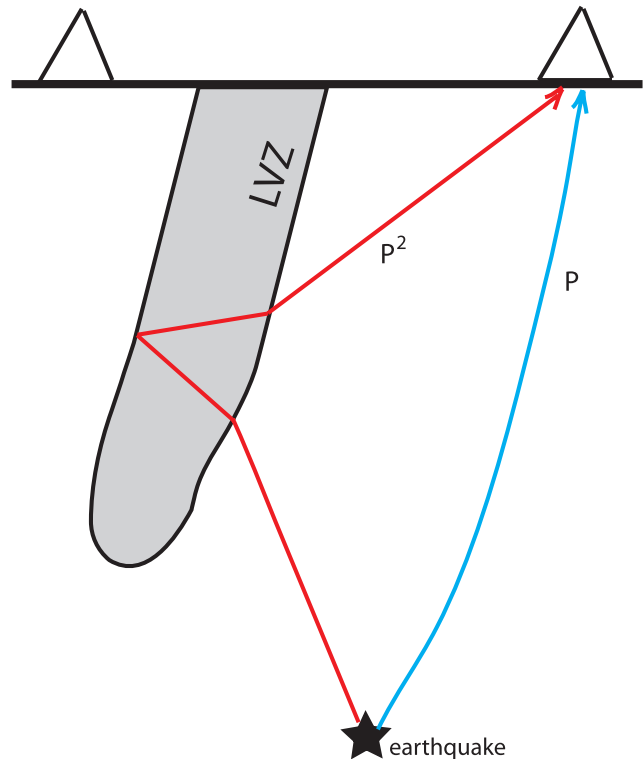


**Figure 4.** A sketch showing the direct (blue) and FZ-reflected (red) *P* waves from an earthquake (star) to station (triangle). LVZ, low velocity zone.

between the direct and FZ-reflected  $P$  and  $S$  waves can be expressed as:

$$P^n - P = nw\sqrt{V_p^{-2} - p^2}, \quad (1)$$

$$S^n - S = nw\sqrt{V_s^{-2} - p^2}, \quad (2)$$

where  $p$  is the ray parameter and  $n$  is the number of ray legs of the multiple reflection in the FZ. This technique has been successfully applied to the Landers FZ using aftershock data of the 1992 Landers

earthquakes. Using the new technique, the trade-off between the LVZ width and velocity drops is greatly reduced (Li *et al.* 2007). The method has, however, some limitations. For example, events have to be close to seismic stations so that the free-surface effect can be easily corrected. In order to use generalized ray theory, we have to ignore depth-dependent variations of host-rock and LVZ structures. When such depth-dependent variations are evident, we use the finite-differences method in the waveform modelling.

We first rotated three component seismograms into the FZ radial, FZ normal and FZ parallel directions (see details in Li *et al.* 2007)

## Event 5850

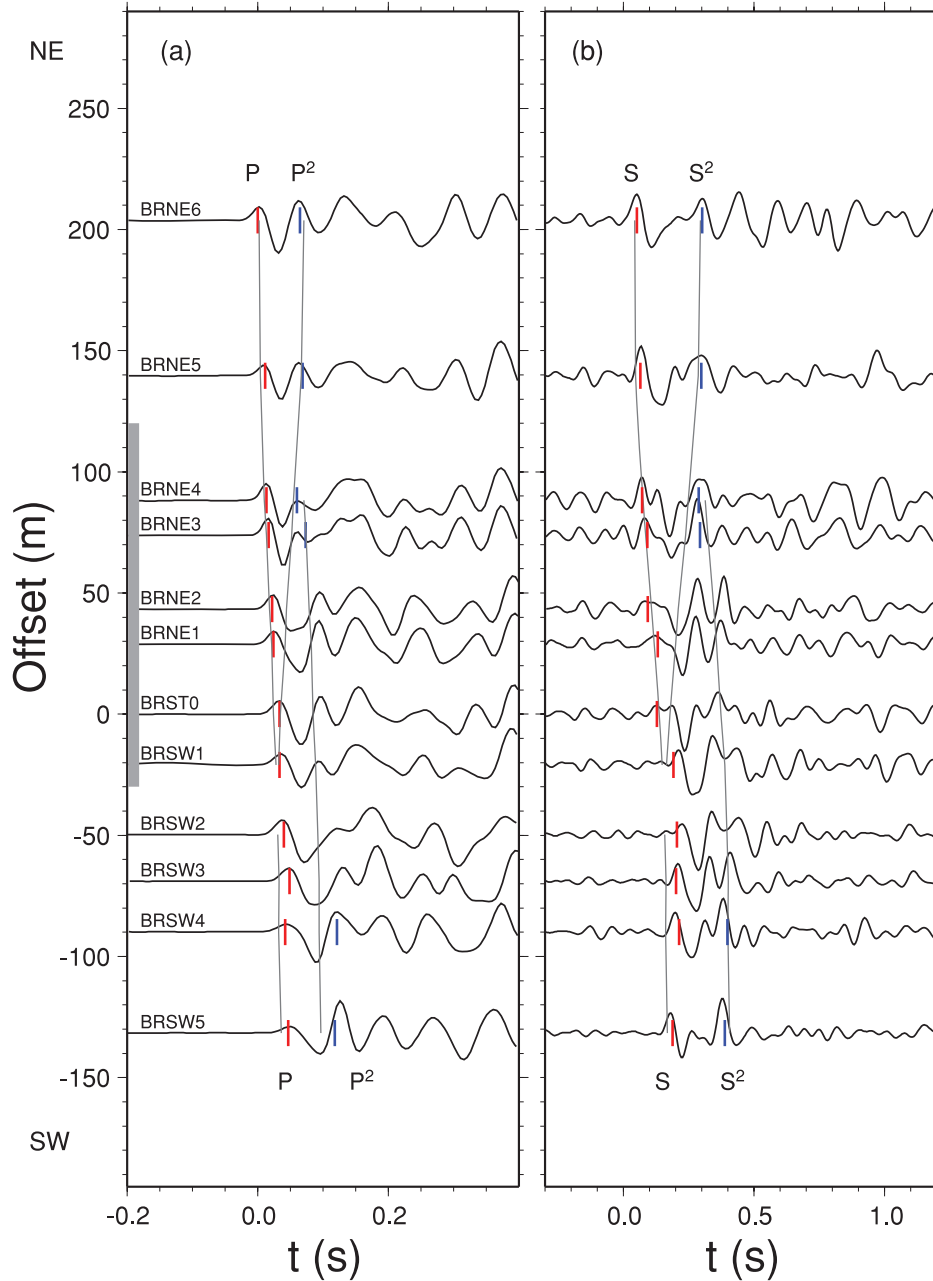


**Figure 5.** Waveform record section of, from left to right, the FZ radial component in  $P$  window and the FZ parallel component in  $S$  window for event 5850 located in the east of the BRF (Fig. 3). The horizontal axes show time after  $P$  arrival at station BRST0 for the radial component and after  $S$  arrival for the FZ parallel components. Red vertical bars represent direct  $P$ - and  $S$ -wave arrival times and blue bars denote available FZ-reflected wave arrivals ( $P^2$  and  $S^2$ ). The lines represent predicted arrival times of direct  $P$  or  $S$  wave and its multiple FZ reflected phases. Vertical grey bar represents location of the LVZ.

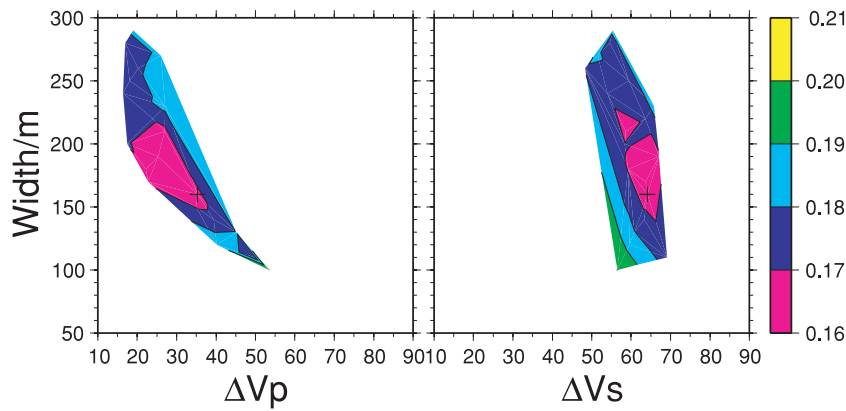


**Figure 6.** FZ width and  $P$ - and  $S$ -wave velocity drops as determined by least-square inversions of direct and FZ-reflected  $P$  and  $S$  arrival times for event 5850. Traveltime residuals in seconds are shown by colour contours and black crosses represent optimal solutions.

using the FZ dip determined above and FZ strike following the surface trace (Fig. 3). Fig. 5 shows a waveform record section from an earthquake located on the northeastern side of the BRF fault trace. A notable feature of the record section is that arrival times of direct  $P$  and  $S$  waves are delayed by  $\sim 0.05$  and  $\sim 0.2$  s, respectively, from the northeastern-most to the southwestern-most stations. The delay starts near station BRNE4 and ends near BRSW1, over a distance of  $\sim 150$  m, indicating existence of a LVZ with its northeastern boundary near BRNE4 and southwestern boundary near BRSW1 that allows us to constrain the LVZ width to be 150 m. The LVZ is not centred at the surface trace (location of station BRST0), but is shifted to the northeast by  $\sim 50$  m. In addition, we identified the FZ-reflected  $P$  and  $S$  waves at some stations (labelled  $P^2$  and  $S^2$  in Fig. 5). The time delays of the FZ-reflected waves relative to the direct arrivals were used to determine the velocity drops of the LVZ compared to the host rock. We fixed the  $V_p$  of host rock to be  $6.3 \text{ km s}^{-1}$  and the  $V_s$  to be  $3.6 \text{ km s}^{-1}$ . The best-estimated LVZ  $P$ -wave velocity drop is 30–40 per cent and  $S$ -wave velocity drop is  $\sim 60$  per cent (Fig. 6). The predicted arrival times of the direct and FZ-reflected waves using the best LVZ model are shown in Fig. 5.

### 3.3 Constrain on LVZ depth by $S_{\text{diff}}$ waves

One interesting feature we found in Fig. 2 is a precursor before the direct  $S$  wave. It only appears at stations on the southwest side of the array and its amplitude decreases at stations close to the FZ (Fig. 2). From FZ wave synthetic tests in the Lander FZ study (Li *et al.* 2007), we showed that the precursors are diffracted  $S$  waves ( $S_{\text{diff}}$  hereafter) (Fig. 7). We also found that the occurrence and amplitudes of LVZ-diffracted wave depend on the LVZ depth (Li *et al.* 2007). Therefore, it could be used to constrain the LVZ depth. In this section we show how it is possible to determine the LVZ depth by modelling the  $S_{\text{diff}}$  waves.

First we set up a 500-m-long hypothetical array with a 20 m station spacing centred across a 200-m-wide LVZ. The LVZ has a north–south orientation and dips  $70^\circ$  to the west (Figs 8a and b). It extends down to a depth of 2 km and has a 50 per cent reduction in  $V_s$  and a 40 per cent reduction in  $V_p$ . The western boundary of the LVZ is located 40 m west of the centre station. Attenuation in the LVZ is set as  $Q_s = 10$  and  $Q_p = 40$  (model 1 in Table 1). The earthquake is located 2.5 km west of the centre station and its depth is 15 km (Location *a* in Figs 8a and b). We computed synthetic waveforms by the finite-differences technique with a grid size of 30 m and time step of 0.002 s. The maximum signal frequency is

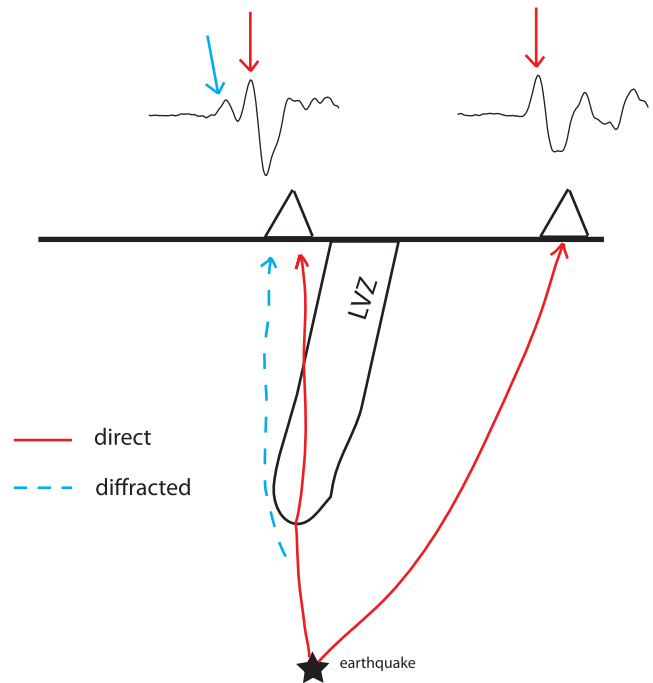


**Figure 7.** Direct (red) and diffracted (blue) waves from an earthquake (star) arrive at two stations (triangles). Two seismograms are shown on the top of stations with red and blue arrows pointing to the direct and diffracted waves. LVZ denotes a low velocity zone embedded into a half-space.

12 Hz. Synthetic waveforms of the transverse component are shown in Fig. 8(d).  $S_{\text{diff}}$  waves appear at the western-side stations of the array. Their amplitudes relative to  $S$  waves decrease towards the FZ and eventually vanish at stations inside the LVZ (Fig. 8d).

We then computed synthetic waveforms for the same event location but for two other different LVZ models of different depths (model 2 and 3 in Table 1) to demonstrate the sensitivity of the  $S_{\text{diff}}$  to LVZ depth. The two LVZ models have the same parameters as the first model but their depths are increased and decreased by 1 km, respectively. We compared synthetic waveforms for different LVZ depths and found that the  $S_{\text{diff}}$  waveforms changed noticeably (Figs 8c and e). The  $S_{\text{diff}}$  are visible at the western stations for all the models. However, their amplitudes relative to the  $S$  wave are quite different. For the LVZ of 2 km deep, the amplitudes of  $S_{\text{diff}}$  are slightly smaller than  $S$  wave (Fig. 8d). When the LVZ depth is decreased from 2 km to 1 km, the  $S_{\text{diff}}$  are very strong and have

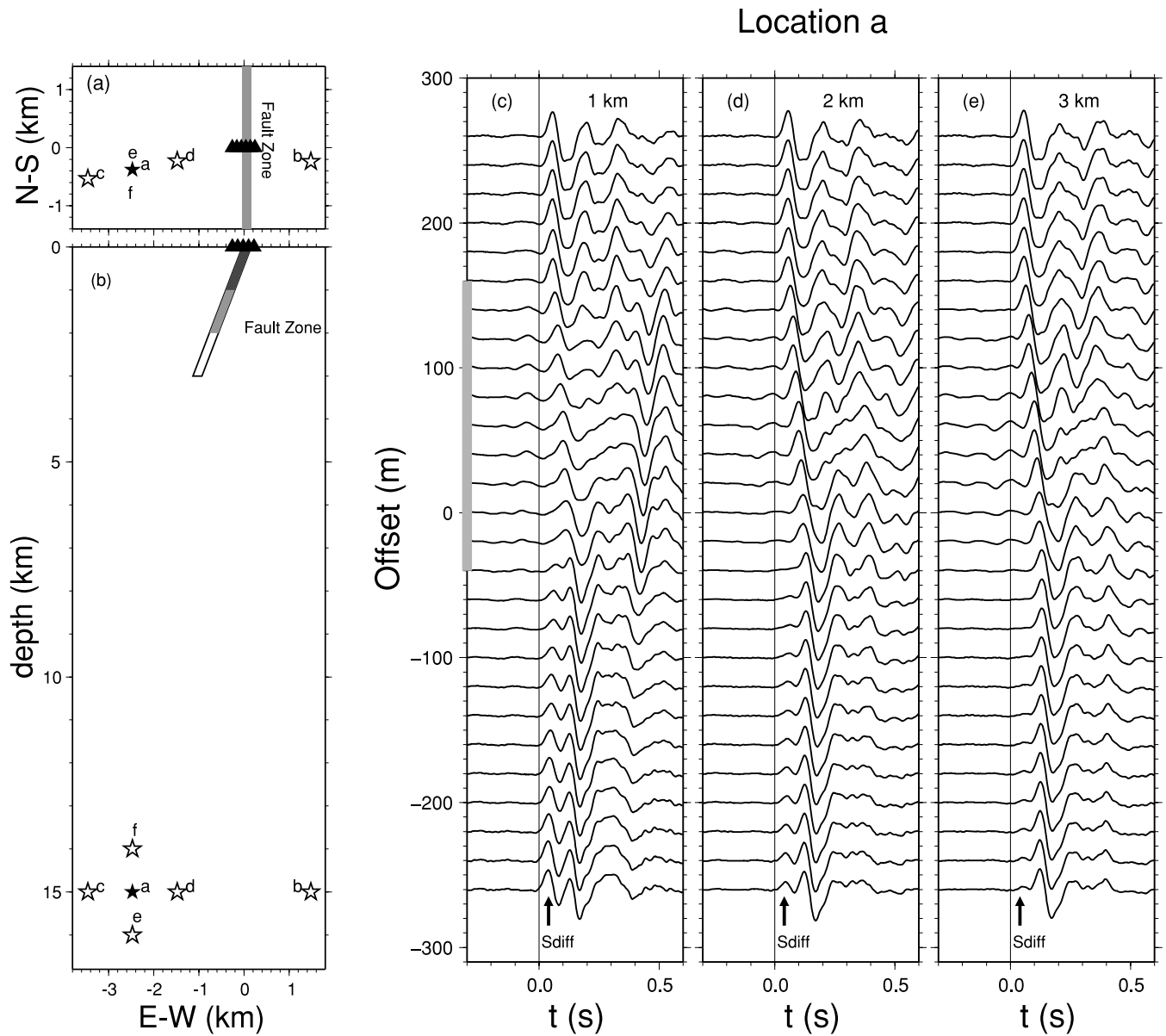


**Figure 8.** (a) Locations of a seismic array (triangles) across a 200 m wide, N–S oriented, and 20° dipping fault zone. Stars denote possible locations of an earthquake. (b) The cross section perpendicular to the FZ strike. Dark grey, grey and white bars represent different LVZ depths. (c), (d) and (e) Synthetic waveforms of transverse component seismograms corresponding to fault zone depths of 1, 2 and 3 km. Black arrows point out the  $S$ -diffracted waves. Event locates at  $a$  position in (a) and (b).

**Table 1.** Different fault zone models used in synthetic test.

M#	Dip (°)	$\Delta V_s$ (per cent)	$\Delta V_p$ (per cent)	$d$ (km)	$W$ (m)	$Q_p$	$Q_s$
1	110	50	40	2	200	40	10
2	110	50	40	1	200	40	10
3	110	50	40	3	200	40	10
4	110	25	40	2	200	40	10

Note:  $\Delta V_s$  and  $\Delta V_p$ ,  $S$ - and  $P$ -wave velocity reduction;  $d$ , fault zone depth;  $W$ , fault zone width.

larger amplitude than the  $S$  wave at most western stations (Fig. 8c). In comparison, we only observed very weak  $S_{\text{diff}}$  when the LVZ depth is 3 km. The  $S_{\text{diff}}$  are only visible at several stations away from the LVZ (Fig. 8e). From these results, we conclude that we are able to resolve the LVZ depth reliably within 1 km, provided that we know the location of the event accurately.

In this study, we selected events located by Shearer *et al.* (2005). Most event locations have relatively small uncertainties both laterally and in depth, usually less than 1 km. However, if combined with uncertainties of other FZ parameters, the event location uncertainties could result in large uncertainties of LVZ depth (Li *et al.* 2007). To consider the effect of event location uncertainties, we perturbed

the event location by 1 km in depth and epicentral distances (Table 2). At each perturbed location, we find the best-fitting LVZ depth by comparing the ‘unperturbed’ waveforms (for an event located at *a* in Figs 8(a) and (b) and a 2-km-deep LVZ) and synthetic at the perturbed event location. Fig. 9(a) shows that the best fit for event location *f* gives a LVZ of 2 km deep, same as the ‘true’ depth. We performed the same procedure for a shallow event depth (location *e* in Figs 8a and b) and found the best-fitting LVZ depth is also 2 km. Therefore, we believe that the uncertainties of event depths has little effects on the LVZ depth by modelling the  $S_{\text{diff}}$  waves.

As we perturbed the event location on epicentral distance, we found that the obtained LVZ depth was more sensitive to the lateral uncertainty of event location. We modeled LVZ depth with the

**Table 2.** Best-fitting LVZ depth corresponding to event locations.

Eve loc	$\Delta$ (km)	$\theta$	$h$ (km)	$d$ (km)
a <sup>1</sup>	2.5	261	15	2
b	1.5	100	15	N/A
c	3.5	261	15	3
d	1.5	261	15	1
e	2.5	261	16	2
f	2.5	261	14	2

*Note:*  $\Delta$ , epicentral distance to the centre station;  $\theta$ , backazimuth to the centre station;  $h$ , event depth;  $d$ , best-fitting LVZ depth.

<sup>1</sup>Initial location of the ‘data’.

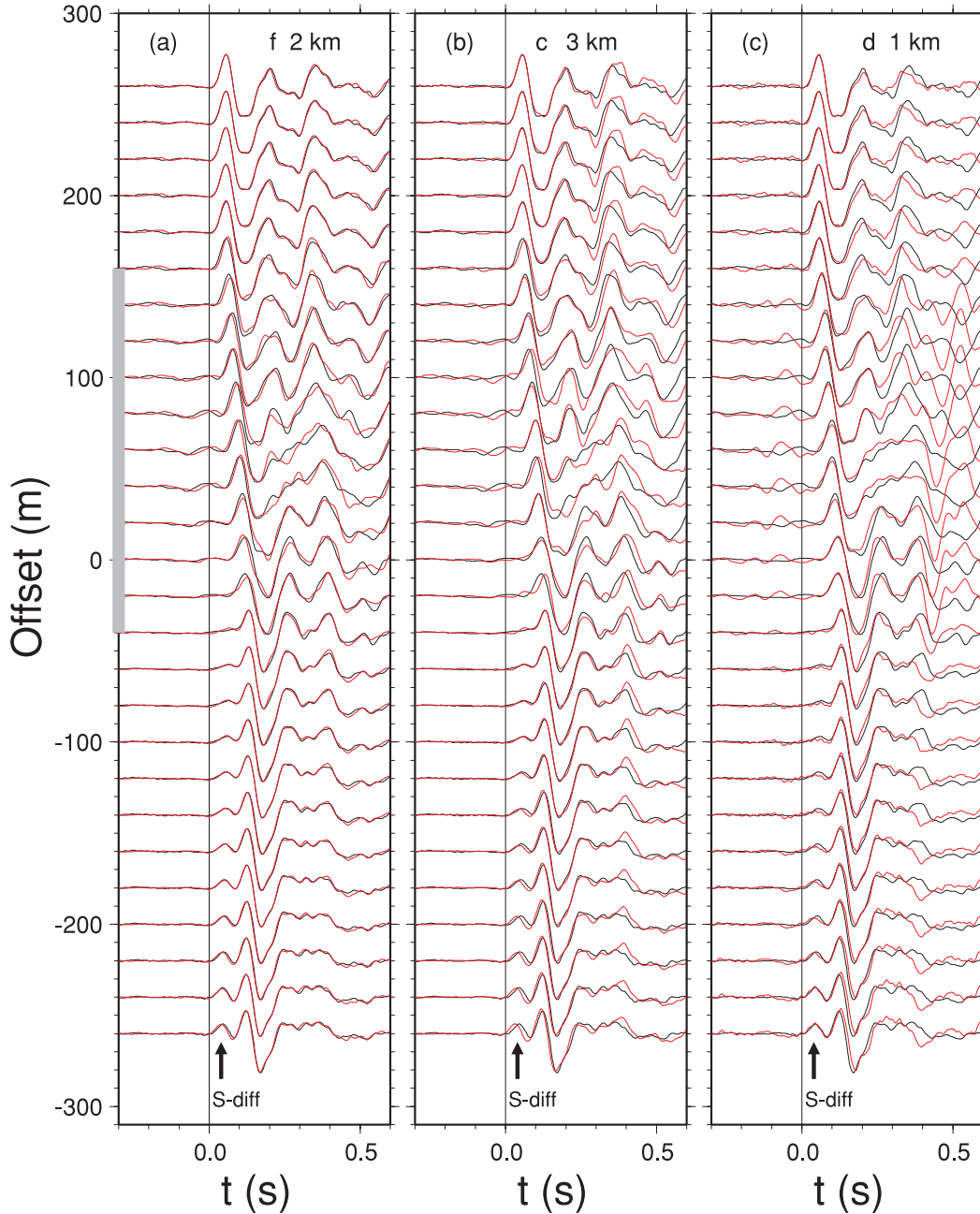


**Figure 9.** Black are synthetic seismograms representing the ‘data’ for an earthquake located at *a* in Figs 8(a) and (b) and the FZ model No. 1 in Table 1. Red traces are synthetic seismogram for earthquakes located at (a) *f*, (b) *c* and (c) *d* in Figs 8(a) and (b). At each location, the best-fitting LVZ depth is (a) 2 km, (b) 3 km and (c) 1 km. Black arrows point to the  $S$ -diffracted phases.

earthquake epicentral distance increased by 1 km (location *c* in Figs 8a and b). The best-fitting LVZ depth is 3 km (Fig. 9b), 1 km larger than the ‘true’ depth. In addition, we found the best-fitting LVZ depth is 1 km for the event epicentral distance decreased by 1 km (location *d* in Figs 8a and b). Therefore, we conclude that uncertainty of LVZ depth using  $S_{\text{diff}}$  is  $\sim 1$  km if uncertainties of event locations are  $\sim 1$  km.

Using the FZ dip, width and velocity reduction determined earlier, we computed synthetic waveforms for LVZ models with different depths by the finite-differences technique. Fig. 10 shows waveform fits of the transverse component for two events. The best-fitting LVZ depth is 2 km and its uncertainties are estimated as 1 km assuming that uncertainties of event locations are no more than 1 km.

#### 4 DISCUSSION AND CONCLUSIONS

In this study, we investigated the SJFZ structure near Anza, southern California, by modelling local earthquake waveforms recorded by three temporary arrays. We found that the LVZ of the BRF has a width of  $\sim 150$  m, dips  $70^\circ$  southwestward, is reduced 50–60 per cent in  $V_s$  and 30–40 per cent in  $V_p$ , and extends  $\sim 2$  km in depth. The width is consistent with results of previous studies (Li *et al.* 1997; Li & Vernon 2001; Lewis *et al.* 2005). The FZ dip agrees with results of analysing locations of earthquakes with FZ trapped waves (Li & Vernon 2001). The *S*-wave velocity reduction is slightly higher than those from the FZ trapped wave study (Li & Vernon 2001; Lewis *et al.* 2005). The LVZ is not centred at the surface trace of the BRF but is shifted to the northeast by

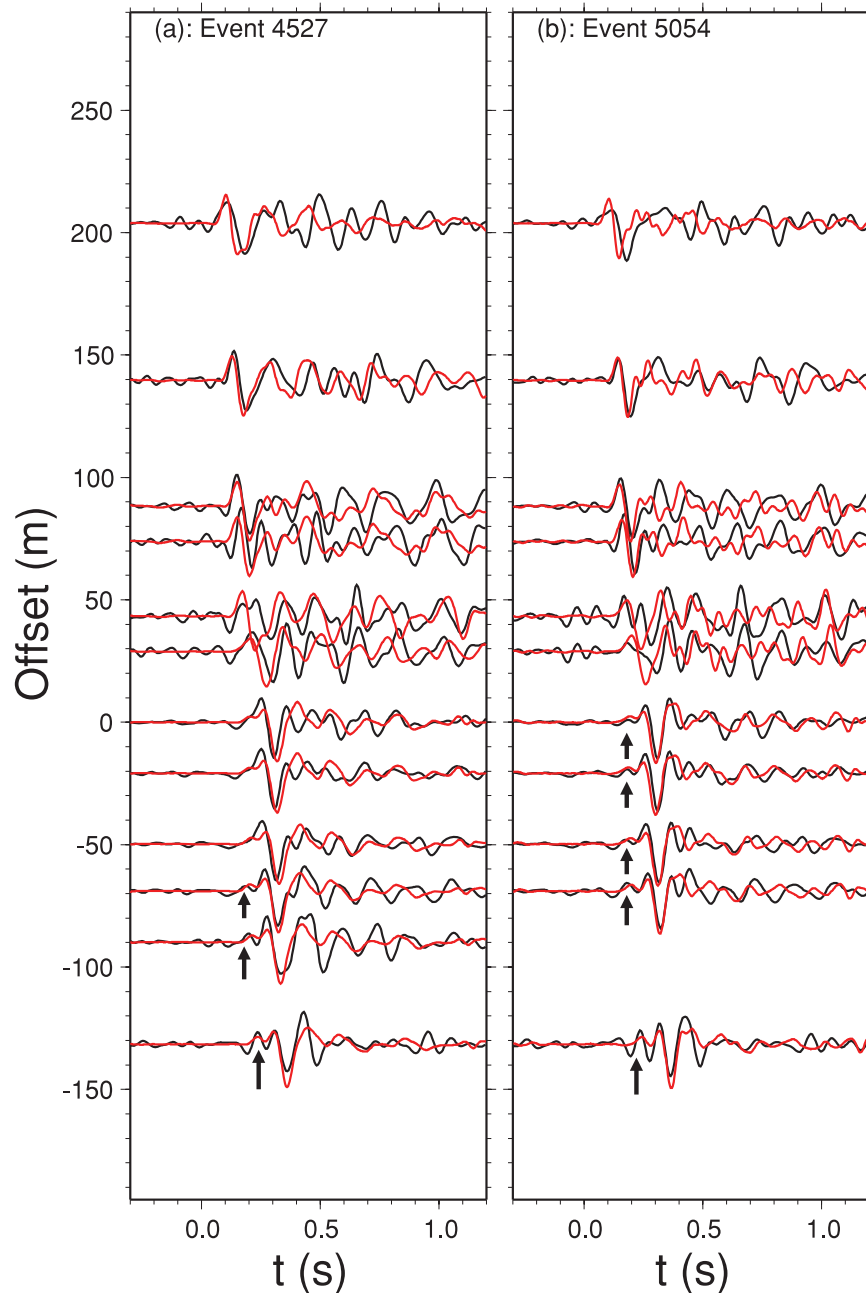


**Figure 10.**  $S$  and  $S_{\text{diff}}$  wave data (black) and synthetic waveforms (red). From left to right, two events, (a) 4527, (b) 5054, recorded by the BRF array. Event locations are shown in Fig. 3(b). Black arrows point to the  $S_{\text{diff}}$  phase.

~50 m, which was also found by the FZ trapped wave study (Lewis *et al.* 2005). We interpret the LVZ to be the cumulative damage zone caused by ruptures of repeated earthquakes in the region over geological time. The SJFZ is seismically active and a few moderate to large magnitude earthquakes occurred since 1890. Mechanisms to reduce seismic wave velocities in the damage zone could include intense fracturing and pulverization, brecciation and fluid saturation (Chester *et al.* 1993). Our results show significant higher reduction in  $V_s$  than in  $V_p$ , suggesting that fluid saturation might be the main mechanism because it affects  $V_s$  more than  $V_p$ .

A central issue in FZ imaging is the depth extent of the low-velocity waveguide zone. One group suggested that it penetrates down to the base of the seismogenic zone (e.g. Li *et al.* 1994, 2000;

Li & Vernon 2001; Li *et al.* 2004), while others argued for a shallow trapping structure extending only to a depth of 3–5 km (e.g. Ben-Zion *et al.* 2003; Peng *et al.* 2003; Lewis *et al.* 2005). A recent numerical analysis of FZ trapped wave pointed out that determination of fault structure at seismogenic depth requires analysis of data at higher frequencies than the FZ trapped wave (Wu *et al.* 2008). In this study, we used precursors before the direct  $S$  waves, the  $S_{\text{diff}}$  waves, which are sensitive to LVZ depth (Li *et al.* 2007). They were used to study some fracture models (Grad 1984), but have not been used to image LVZ depth so far. Our synthetic tests show that the  $S_{\text{diff}}$  waves are suitable to determine LVZ depth because their relative amplitudes to the direct  $S$  waves are very sensitive to depth of the LVZs. Our modelling results show that the LVZ of the BRF

## 19990411003531

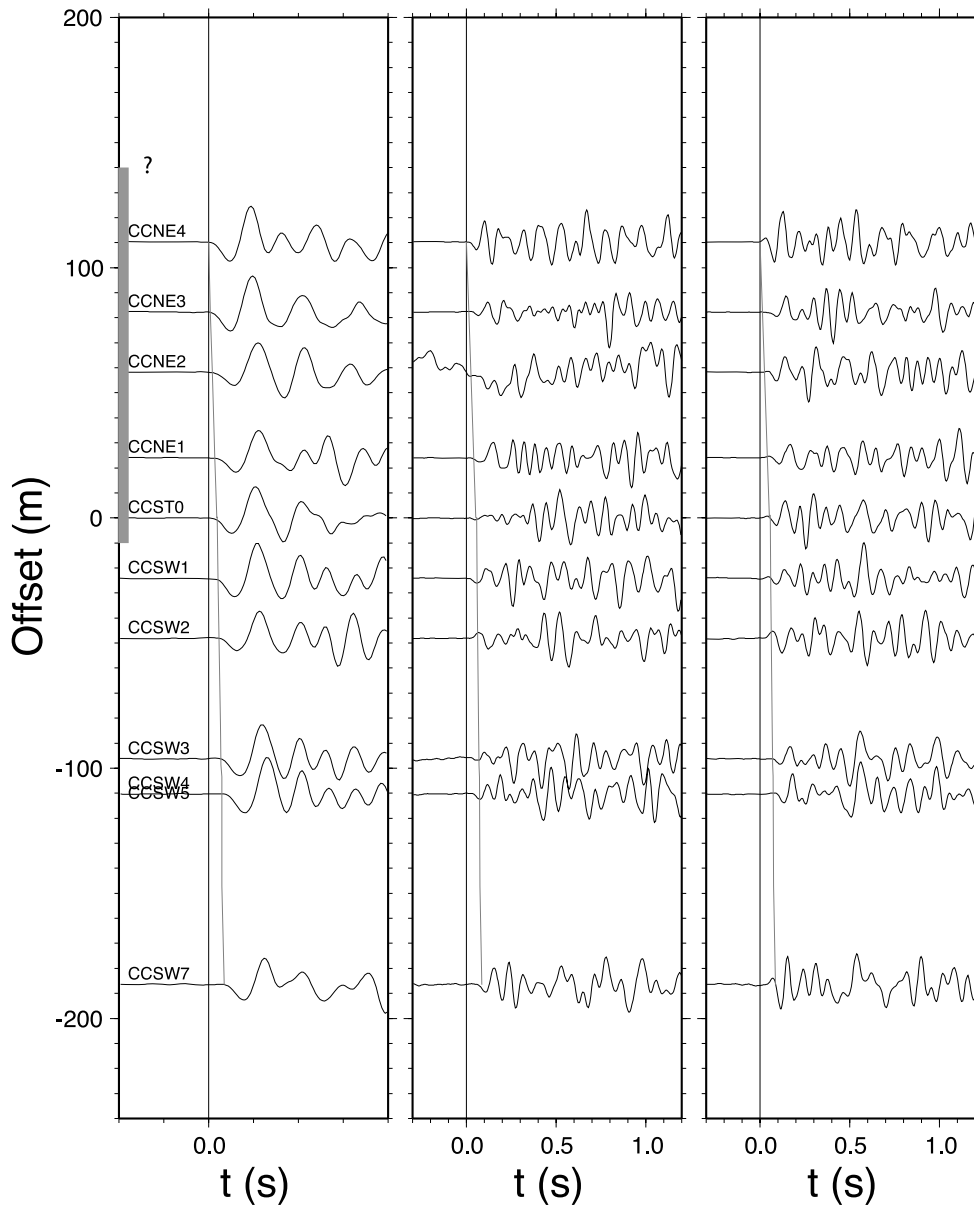


**Figure 11.** Three-component seismograms of event 3531 recorded by the seismic array across the CCF. Same to Fig. 2, from left to right are vertical component in  $P$  window, radial, and horizontal components in  $S$  window. The  $Y$ -axis stands for the offset from the central station of the array from southwest to northeast. Lines represent predicted arrival times from the obtained model. Thick grey line shows location of the LVZ.

extends 2 km in depth that is consistent with the proposed shallow structure of Lewis *et al.* (2005). The depth uncertainties are estimated by the synthetic tests in which we believe the uncertainties of FZ depth are in the same order with the uncertainty of event locations (especially in lateral distance). Since most event locations used in this study have uncertainties less than 1 km (Shearer *et al.* 2005), we believe the uncertainties of the LVZ depth of the BRF is less than 1 km.

During our waveform modelling and synthetic tests, we assumed that the FZ was a simple tabular layer embedded in a half-space. The newly developed technique (Li *et al.* 2007) could take into account the effect of gradational reduction of seismic velocities from host rock to the LVZ. The gradation will not significantly affect the waveforms in the frequency band (1–15 Hz) that we used unless the gradient zone is more than  $\sim 100$  m. In addition, the FZ structure is not variant with depth. However, most FZs are not that simple and their properties are depth dependent. For instance, the Calico FZ in California has a depth-dependent velocity reduction, 50 per cent reduction in  $V_s$  down to 5 km and gradually changed to 25 per cent from 5 to 10 km (Cochran *et al.* 2009). We could not exclude the case that the LVZ of the BRF extends to 2 km in depth with a 50–60 per cent reduction in  $V_s$  and extends further down with much smaller velocity contrast or width. For example, Hong and Menke [2006] suggested that low shear velocities of 6–8 per cent in the San Jacinto FZ were observed down to a depth of  $\sim 16$  km. We performed a synthetic test for a FZ model with 25 per cent reduction in  $V_s$  (model 4 in Table 1). The model grid size was set to 30 m which corresponds to 15 Hz in signal frequency. We did not observe any diffracted waves. In order to resolve fine structure, we had to compute with smaller grid size to get higher frequency which requires much longer CPU time and larger memory usage.

We did not find clear signature of FZ-reflected and diffracted waves for the CVF and the CCF branches (Fig. 11). Due to the nature of diffraction, the FZ diffracted waves can only be seen in certain event-station geometry related to the shape of LVZ. The number of events recorded by the CVF and CCF arrays is small. The LVZs of CVF and CCF are probably less developed than the BRF's. Based on traveltimes modelling alone, we estimated that the CCF has a LVZ of  $\sim 150$  m in width and of 50 per cent reduction in  $V_s$  and 25 per cent reduction in  $V_p$ . The LVZ of the CVF is  $\sim 200$  m in width and has 50 per cent reduction in  $V_s$  and 40 per cent reduction in  $V_p$ . The results are consistent with the previous studies (Li & Vernon 2001; Lewis *et al.* 2005). However, there might be a strong trade-off between the LVZ width and velocity drop because we did not have constraint from FZ-reflected waves.

In summary, we investigated fine structure of the SJFZ near Anza, southern California, by modelling high frequency body waves. We found that the LVZ associated with the BRF is  $\sim 150$  m in width and has a 30–40 per cent reduction of  $V_p$  and a 50–60 per cent reduction of  $V_s$ . The BRF is dipping  $70 \pm 5^\circ$  southwest and its depth extent is  $2 \pm 1$  km. It is not centred on the surface fault trace but is shifted  $\sim 50$  m to the northeast, implying the asymmetric damage during earthquakes.

## ACKNOWLEDGMENTS

The authors thank editor Jean Virieux and three anonymous reviewers for their valuable comments to improve the manuscript greatly. The authors also thank Dr. Yehuda Ben-Zion at University of Southern California and Dr. Frank Vernon at University of California, San Diego for providing waveform data. This work is supported by the National Science Foundation under Grant No. EAR-0609969.

## REFERENCES

- Aki, K., 1979. Characterization of barriers on an earthquake fault, *J. geophys. Res.*, **84**, 6140–6148.
- Becker, T.W., Hardebeck, J.L. & Anderson, G., 2005. Constraints on fault slip rates of the southern California plate boundary from GPS velocity and stress inversions, *Geophys. J. Int.*, **160**, 634–650.
- Ben-Zion, Y. & Aki, K., 1990. Seismic radiation from an SH line source in a laterally heterogeneous planar fault zone, *Bull. seism. Soc. Am.*, **80**, 971–994.
- Ben-Zion, Y. & Malin, P., 1991. San Andreas fault zone head wave near Parkfield, California, *Science*, **251**, 1592–1594.
- Ben-Zion, Y. & Sammis, C.G., 2003. Characterization of fault zones, *Pure appl. Geophys.*, **160**, 677–715.
- Ben-Zion, Y. & Shi, Z., 2005. Dynamic rupture on a material interface with spontaneous generation of plastic strain in the bulk, *Earth planet. Sci. Lett.*, **236**, 486–496.
- Ben-Zion, Y., Katz, S. & Leary, P., 1992. Joint inversion of fault zone head waves and direct P arrivals for crustal structure near major faults, *J. geophys. Res.*, **97**, 1943–1951.
- Ben-Zion, Y. *et al.*, 2003. A shallow zone structure illuminated by trapped waves in the Karadere-Duze branch of the North Anatolian Fault, western Turkey, *Geophys. J. Int.*, **155**, 1021–1041.
- Bleibinhaus, F., Hole, J.A., Ryberg, T. & Fuis, G.S., 2007. Structure of the California Coast Ranges and San Andreas fault at SAFOD from seismic waveform inversion and reflection imaging, *J. geophys. Res.*, **112**, B06315, doi:10.1029/2006JB004611.
- Chester, F.M., Evans, J.P. & Biegel, R.L., 1993. Internal structure and weakening mechanisms of the San Andreas fault, *J. geophys. Res.*, **98**, 771–786.
- Cochran, E.S., Li, Y., Shearer, P.M., Barbot, S., Fialko, Y. & Vidale, J.E., 2009. Seismic and geodetic evidence for extensive, long-lived fault damage zones, *Geology*, **37**, 315–318, doi:10.1130/G25306A.1.
- Dor, O., Rockwell, T.K. & Ben-Zion, Y., 2006. Geological observations of damage asymmetry in the structure of San Jacinto, San Andreas and Punchbowl faults in southern California: a possible indicator for preferred rupture propagation direction, *Pure appl. geophys.*, **163**, 301–349.
- Eberhart-Phillips, D., Stanley, W.D., Rodriguez, B.D. & Lutter, W.J., 1995. Surface seismic and electrical methods to detect fluids related to faulting, *J. geophys. Res.*, **97**, 12 919–12 936.
- Evans, J.P. & Chester, F.M., 1995. Fluid-rock interaction in faults of the San Andreas system: inferences from San Gabriel fault rock geochemistry and microstructures, *J. geophys. Res.*, **100**(B7), 13 007–13 020.
- Grad, M., 1984. Reflected-diffracted waves in fracture zone models, *Geophys. J. Int.*, **79**, 353–361.
- Hole, J.A., Catchings, R.D., Clair, K., C.S., Rymer, M.J., Okaya, D.A. & Carney, B.J., 2001. Steep-dip seismic imaging of the shallow San Andreas Fault near Parkfield, *Science*, **294**, 1513–1515.
- Johnson, A.M., Fleming, R.W. & Cruikshank, K.M., 1994. Shear zones formed along long, straight traces of fault zones during the 28 June 1992 Landers, California earthquake, *Bull. seism. Soc. Am.*, **84**, 499–510.
- Kanamori, H., 1994. Mechanics of earthquakes, *Ann. Rev. Earth Planet. Sci.*, **22**, 207–237.
- Kanamori, H. & Brodsky, E.E., 2004. The physics of earthquakes, *Rep. Prog. Phys.*, **67**, 1429–1496.
- Korneev, V.A., Nadeau, R.M. & McEvilly, T.V., 2003. Seismological studies at Parkfield IX: fault-zone imaging using guided wave attenuation, *Bull. seism. Soc. Am.*, **93**, 1415–1426.
- Lewis, M.A., Peng, Z.G., Ben-Zion, Y. & Vernon, F.L., 2005. Shallow seismic trapping structure in the San Jacinto fault zone near Anza, California, *Geophys. J. Int.*, **162**, 867–881.
- Li, H., Zhu, L. & Yang, H., 2007. High-resolution structures of the Landers fault zone inferred from aftershock waveform data, *Geophys. J. Int.*, **171**, doi:10.1111/j.1365-246X.2007.03608.x.
- Li, Y. & Malin, P.E., 2008. San Andreas Fault damage at SAFOD viewed with fault-guided waves, *Geophys. Res. Lett.*, **35**, L08304, doi:10.1029/2007GL032924.

- Li, Y.G. & Vernon, F.L., 2001. Characterization of the San Jacinto fault zone near Anza, California, by fault zone trapped waves, *J. geophys. Res.*, **106**, 30 671–30 688.
- Li, Y.G., Aki, K., Adams, D., Hasemi, A. & Lee, W.H.K., 1994. Seismic guided waves trapped in the fault zone of the Landers, California, earthquake of 1992, *J. geophys. Res.*, **99**, 11 705–11 722.
- Li, Y.G., Vernon, F.L. & Aki, K., 1997. San Jacinto fault-zone guided waves: a discrimination for recently active fault strands near Anza, California, *J. geophys. Res.*, **102**, 11 689–11 701.
- Li, Y.G., Vidale, J.E., Aki, K., Xu, F. & Burdette, T., 1998. Evidence of shallow fault zone strengthening after the 1992 *M* 7.5 Landers, California, earthquake, *Science*, **279**, 217–219.
- Li, Y.G., Vidale, J.E., Aki, K. & Xu, F., 1999. Shallow structure of the Landers fault zone from explosion-generated trapped waves, *J. geophys. Res.*, **104**, 20 257–20 275.
- Li, Y.G., Vidale, J.E., Aki, K. & Xu, F., 2000. Depth-dependent structure of the Landers fault zone using fault zone trapped waves generated by aftershocks, *J. geophys. Res.*, **105**, 6237–6254.
- Li, Y.G., Vidale, J.E., Day, S.M., Oglesby, D.D. & the, SCEC Field Working Team, 2002. Study of the 1999 *M* 7.1 Hector Mine, California, earthquake fault plane by trapped waves, *Bull. seism. Soc. Am.*, **92**, 1318–1332.
- Li, Y.G., Vidale, J.E., Oglesby, D.D., Day, S.M. & Cochran, E., 2003. Multiple-fault rupture of the *M* 7.1 Hector Mine, California, earthquake from fault zone trapped waves, *J. geophys. Res.*, **108**, doi:10.1029/2001JB0014563.
- Li, Y.G., Vidale, J.E. & Cochran, E.S., 2004. Low-velocity damaged structure of the San Andreas Fault at Parkfield from fault zone trapped waves, *Geophys. Res. Lett.*, **31**, L12S06, doi:10.1029/2003GL019044.
- Lutz, A.T., Dorsey, R.J., Housen, B.A. & Janecke, S.U., 2006. Stratigraphic record of Pleistocene faulting and basin evolution in the Borrego Badlands, San Jacinto fault zone, Southern California, *Geol Soc Am Bull.*, **118**(11–12), 1377–1397, doi:10.1130/B25946.1.
- McGuire, J. & Ben-Zion, Y., 2005. High-resolution imaging of the Bear Valley section of the San Andreas fault at seismogenic depths with fault-zone head waves and relocated seismicity, *Geophys. J. Int.*, **163**, 152–164, doi:10.1111/1365-246X.2005.02703.x.
- Mooney, W.D. & Ginzburg, A., 1986. Seismic measurements of the internal properties of fault zones, *Pure appl. Geophys.*, **124**, 141–157.
- Peng, Z., Y. Ben-Zion, Michael, A.J. & Zhu, L.P., 2003. Quantitative analysis of seismic fault zone waves in the rupture zone of the Landers, 1992, California earthquake: evidence for a shallow trapping structure, *Geophys. J. Int.*, **155**, 1021–1041.
- Prejean, S., Ellsworth, W., Zoback, M. & Waldhauser, F., 2002. Fault structure and kinematics of the Long Valley Caldera region, California, revealed by high-accuracy earthquake hypocenters and focal mechanism stress inversions, *J. geophys. Res.*, **107**, 2355, doi:10.1029/2001JB001168.
- Rockwell, T., Loughman, C. & Merifield, P., 1990. Late Quaternary rate of slip along the San Jacinto fault zone near Anza, southern California, *J. geophys. Res.*, **95**(B6), 8593–8605.
- Rovelli, A., Caserta, A., Marra, F. & Ruggiero, V., 2002. Can seismic waves be trapped inside an inactive fault zone? The case study of Nocera Umbra, central Italy, *Bull. seism. Soc. Am.*, **92**, 2217–2232.
- Sanders, C.O. & Kanamori, H., 1984. A seismotectonic analysis of the Anza seismic gap, San Jacinto fault zone, southern California, *J. geophys. Res.*, **89**, 5873–5890.
- Scholz, C.H., 1990. *The Mechanics of Earthquakes and Faulting*, Cambridge Univ. Press, New York.
- Shearer, P., Hauksson, E. & Lin, G., 2005. Southern California hypocenter relocation with waveform cross-correlation, Part 2: results using source-specific station terms and cluster analysis, *Bull. seism. Soc. Am.*, **95**, 904–915, doi:10.1785/0120040168.
- Sieh K., *et al.*, 1993. Near-field investigations of the Landers earthquake sequence, April to July 1992, *Science*, **260**, 171–176.
- Sykes, L. & Nishenko, S., 1984. Probabilities of occurrence of large plate rupturing earthquakes for the San Andreas, San Jacinto and Imperial faults, California, *J. geophys. Res.*, **89**(B7), 5905–5928.
- Vidale, J.E. & Li, Y.G., 2003. Damage to the shallow Landers fault from the nearby Hector Mine earthquake, *Nature*, **421**, 524–526.
- Waldhauser, F. & Ellsworth, W.L., 2002. Fault structure and mechanics of the Hayward fault, California, from double-difference earthquake locations, *J. geophys. Res.*, **107**, 2054, doi:1029/2001JB000084.
- Wu, J., Hole, J.A., Snoke, J.A. & Imhof, M.G., 2008. Depth extent of the fault-zone seismic waveguide: effects of increasing velocity with depth, *Geophys. J. Int.*, **173**, doi:10.1111/j.1365-246X.2008.03755.x.
- Yang, H., Zhu, L. & Chu, R., 2009. Fault-plane determination of the 18 April 2008 Mt. Carmel, Illinois, earthquake by detecting and relocating aftershocks, *Bull. seism. Soc. Am.*, **99**(6), 3413–3420, doi:10.1785/0120090038.
- Zhao, P. & Peng, Z., 2008. Velocity contrast along the Calaveras fault from analysis of fault zone head waves generated by repeating earthquakes, *Geophys. Res. Lett.*, **35**, doi:10.1029/2007GL031810.